

# We are IntechOpen, the world's leading publisher of Open Access books Built by scientists, for scientists

6,900

Open access books available

186,000

International authors and editors

200M

Downloads

Our authors are among the

154

Countries delivered to

TOP 1%

most cited scientists

12.2%

Contributors from top 500 universities



WEB OF SCIENCE™

Selection of our books indexed in the Book Citation Index  
in Web of Science™ Core Collection (BKCI)

Interested in publishing with us?  
Contact [book.department@intechopen.com](mailto:book.department@intechopen.com)

Numbers displayed above are based on latest data collected.  
For more information visit [www.intechopen.com](http://www.intechopen.com)



---

# Progress in Experimental Research of Turbine Aeroacoustics

---

Andreas Marn, Christian Faustmann and  
Thorsten Selic

Additional information is available at the end of the chapter

<http://dx.doi.org/10.5772/62431>

---

## Abstract

Modifications on the intermediate turbine duct in order to reduce noise emissions by changing interaction frequencies and/or modes capable to propagate are presented. Also different turbine exit casings are described that are optimised to reduce interaction noise that is propagating through the engine and is one of the major noise sources during landing (operating point approach). The most promising modifications to reduce sound power levels are described. Depending on different modifications at specific operating points, the reduction of sound power level is between 5 dB and 10 dB, which is a significant reduction. However, some of these measures show an increase in aerodynamic losses. Therefore, a compromise has to be found between higher losses during a short duration (e.g. landing) and significant noise reduction. The chapter focuses on experimental results obtained in the test facilities of the Institute for Thermal Turbomachinery and Machine Dynamics at Graz University of Technology.

**Keywords:** aeroacoustics, low pressure turbine, high pressure turbine, turbine exit casing, intermediate turbine duct

---

## 1. Introduction

In modern commercial high bypass ratio aero engines, low specific fuel consumption together with low life cycle costs are mandatory to allow air transportation economically. Furthermore, an environmentally friendly aero engine should have reduced CO<sub>2</sub> emission by even lower fuel burn and generate low noise levels during takeoff (side line and cut back) and landing.

---

At the beginning of the jet era noise emissions were dominated by jet mixing noise. That has been reduced when introducing modern bypass engines by lowering the jet speed. Noise emitted by fan, turbine, and compressor has then become important with the reduction in jet speed. Now, that noise has to be reduced significantly. Since the publication of the ACARE goals, which are targets defined by the Advisory Council for Aeronautics Research in Europe to reduce the environmental impact of air transportation, the commercial and political pressure to reduce CO<sub>2</sub>, NO<sub>x</sub> and noise (up to 20 dB reduction of noise level until 2020 compared to technologies of the year 2000) has been increased considerably. A lot of research over the past decades was done reducing fan and compressor noise in order to achieve the noise reduction targets. During the last years, noise emission from the fan was much reduced that suddenly noise from the interaction of the last stage low pressure turbine and the turbine exit guide vane of the exit casing became perceivable. Nowadays also manufacturers of low pressure turbine components have to consider acoustic aspects in their design to be able to reach the ACARE goals in 2020. Therefore a lot of research is currently done in that field of expertise. An additional benefit of that low noise levels is that passengers as well as residents living in the vicinity of airports feel more comfortable. Basically an increasing acceptance to live close to airports and rise of life quality can be achieved if the noise level of aero engines is decreased significantly.

In this chapter measures to reduce noise generated and propagating from modern aero engine turbines are presented. The main issue is to find methods and/or new engine designs that reduce noise without causing considerable losses or a reduction of thrust. However, a lot of novel engine architectures are investigated in several national and international funded projects with the goal to reduce the emission of pollutants, e.g. by lowering the engine weight. This can be achieved by reducing the length of the entire engine by reducing the axial spacing between blade rows or integrating additional functions in one part, e.g. a non-lifting strut in an intermediate turbine duct which also has to turn the flow and provide the next rotor with the correct inflow conditions. This leads to a so-called turning mid turbine frame. However, all modifications on these parts of the engine will influence the noise generation and propagation. Also a considerable change of excitation of blades and vanes can be observed.

## 2. Experimental setups and test facilities

The Institute for Thermal Turbomachinery and Machine Dynamics at Graz University of Technology operates a 3 MW compressor station in order to supply a couple of test facilities continuously with pressurized air. Among them are the subsonic test turbine facility for aerodynamic, acoustic, and aeroelastic investigations (STTF-AAAI) as well as the two-spool Transonic Test Turbine Facility (TTTF).

### 2.1. Subsonic test turbine facility for aerodynamic, acoustic, and aeroelastic investigations

In the described subsonic turbine test facility for aerodynamic, acoustic and aeroelastic investigations (STTF-AAAI), the maximum pressure ratio is limited to 2 due to the inlet spiral casing. The mass flow rate is limited to 15 kg/s due to the compressor station characteristic. A

temperature at stage inlet of max. 100°C can be realised. This inlet temperature can be adjusted within a wide range by means of water air coolers. The pressurized air enters the facility through a spiral inlet casing where the flow is turned into axial direction. That spiral inlet casing also supports the front bearing of the overhung-type turbine shaft. The shaft is coupled to a water brake counteracting the power of the turbine. The necessary cooling water cycle of the brake is connected to the re-cooling plant of the institute.

For a test rig it is mandatory to provide well-defined and uniform inflow conditions; therefore a de-swirler and a perforated plate are located far upstream of the inlet guide vanes. That mentioned inlet guide vanes upstream of the stage (and downstream of the perforated plate) simulate additional wakes of other upstream low pressure turbine stages. The air leaves the test rig through a cylindrical acoustic measurement section, supporting struts centring the acoustic measurement section, exhaust casing, and the exhaust stack to ambient. For more information a detailed description of the subsonic test turbine facility can be found in Ref. [1].

### 2.1.1. Turbine stage and turbine exit casings[SEQA1]

During the aerodynamic design process it was crucial to achieve relevant model parameters to reproduce the full scale low pressure turbine (LPT) configuration. The diameter of the test rig rotor is about half of that of a commercial aero engine LPT. Therefore the rig is operated at higher rotational speeds to realise an engine relevant loading parameter. A meridional section of the rig is shown in **Figure 1**. The state-of-the-art (reference) and the leaned turbine exit casing (TEC) are shown in the sketch at the top (a). The inverse cutoff as well as the high lift design (H-TEC) can be seen at the bottom (b). It has to be mentioned that the bladings are not drawn to scale. The rig is characterised by a high aspect ratio unshrouded low pressure turbine rotor followed by the TEC. Relevant geometry parameters can be seen in the upper half of **Table 1**.

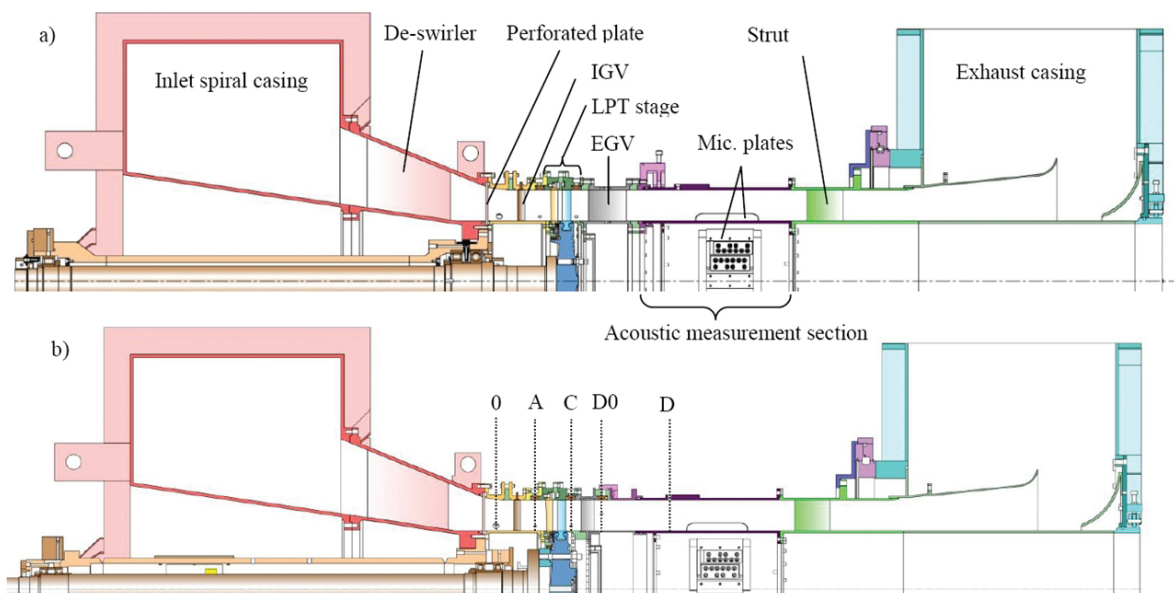


**Figure 1.** Meridional section of the STTF-AAAI; (a) reference and leaned TEC and (b) inverse cutoff and H-TEC.

Four different TEC setups with different vane counts (see **Table 1**) have been tested but the leading edge is at the same axial position for all configurations. One significant difference is that the reference and leaned TEC are manufactured without fillets while the TECs with smaller chord length have fillets at hub and tip due to manufacturing and assembly requirements. The leaned TEC was optimised (detailed information can be found in Ref. [2]) in order to reduce rotor-TEC interaction noise by keeping the profiles of the turbine exit guide vanes (TEGV) to be able to lead through the same supply lines as through the reference TEC. As it was shown in some European projects, e.g. DREAM, the rear bearing can move forward under the TCF section for future engine architectures giving the designer the opportunity to aerodynamically and/or acoustically optimise the vanes of the turbine exit casing. Therefore, the third setup is an acoustically optimised TEC named inverse cutoff TEC. The basic idea of that setup is to utilise a small cutoff corridor in between two cuton regions. A detailed description can be found in Ref. [3] and a verification and comparison with experimental results is given in Ref. [4]. The fourth setup is aerodynamically optimised and is designed to reduce losses at aero design point.

Further, the rig has some inlet guide vanes (IGV) in order to impose some typical pre-swirl on the flow. Stator vanes are located downstream of the IGVs, followed by the rotor and the turbine exit guide vanes (TEGV). The 1 and 1/2 stage is representative of the last stage of a commercial engine with TEGV. **Table 1** shows the blade count and the main geometrical details of the turbine. The rig in its current setup is characterized by a high aspect ratio unshrouded rotor followed by one of the above described turbine exit casings. The tip leakage flow dominates the flow field downstream of the rotor. The flow through the guide vanes is mainly influenced by secondary flows. The TEGV are designed to turn the swirling flow into an axial direction (reducing swirl and lower the kinetic energy of the flow) and to recover some static pressure.

Additionally, for this test rig, a second stator and low pressure turbine rotor has been designed. Stator and rotor have the same blade count as the reference design, but different profile geometries, including a rotor with a 20% increased loading parameter. The design intent of that second stage was to provide a similar/identical rotor exit flow as well as shaft power of the test rig. Because of the larger turning of that highly loaded rotor, the operating points must have been adjusted. A lower rotational speed in order to keep the power output identical was chosen. However, the stage pressure ratio has been kept the same as for the datum stage. There have been two reasons to keep the blade and vane counts identical. Firstly, it is the geometrical limitation of the test rig. Axial chord of both stator and rotor had to be the same as well as the axial distance between the vanes and blades. Secondly, the resulting acoustic and aerodynamic field is dependent on the number of blades and vanes of the test rig [5]. In order to keep the modal structure of the blade/vane interactions the same as for the datum stage, the number of blades and must be the same.

### *2.1.2. Operating conditions*

Because the STTF-AAAI is used for both acoustic and aerodynamic investigations, the main operating points are selected according to relevant noise certification points. They have been

defined using a typical aerodynamic design point of a last stage of an LPT. That design point is derived from current LPT design practice and scaled along reduced speed, reduced mass flow (both referred to 288.15 K and 1013.25 mbar) and pressure ratio. For this investigation the acoustically relevant operating point approach was chosen. The Reynolds number of the TEGVs is defined using the midspan conditions at rotor exit as well as the axial chord of the vanes. The lower half of **Table 1** shows the operating conditions.

<b>Geometry details</b>	
<b>Number of blades/vanes</b>	
IGV/Stator/Rotor/	83/96/72
TEGV state-of-the-art (Reference TEC)	15
TEGV leaned TEC	15
TEGV inverse cutoff (inv.)	>40
TEGV H-TEC	<35
Tip gap to blade height ratio	1.0%
Hub to tip radius ratio	≈2/3
<b>Operating conditions</b>	
TEGV Reynolds number ratio $Re_{ref.}/Re_{H-TEC}$	~3
TEGV Reynolds number ratio $Re_{ref.}/Re_{inv.}$	~3
TEGV Reynolds number ratio $Re_{ref.}/Re_{leaned}$	~1
Diffusion factor ref./leaned/inv./H-TEC	~0.5/~0.5/~0.6/~0.6
Reduced mass flow	6.94 kg/s
Reduced rotational speed	3653 rpm/4060 rpm
Stage pressure ratio	1.16
Stage total inlet temperature	100°C

**Table 1.** Geometry details and operating conditions.

## 2.2. Transonic test turbine facility

The setups being tested consist of a single-stage unshrouded transonic HP turbine. Downstream of that turbine stage, a S-shaped turbine centre frame, which is the main part of interest for this investigation, is located. The centre frame is followed by a shrouded counter-rotating LPT rotor (see **Figure 2**). The pressurized air flows through the transonic unshrouded HPT rotor and enters the turbine centre frame. The air is then turned by 16 struts in the turbine centre frame (resulting in a turning mid turbine frame [TMTF]) in negative direction relative to the rotation of the HP rotor. After that the air enters the LP rotor at a larger diameter and with an appropriate swirl angle. Blading parameters and operating conditions can be seen in **Table 2**.

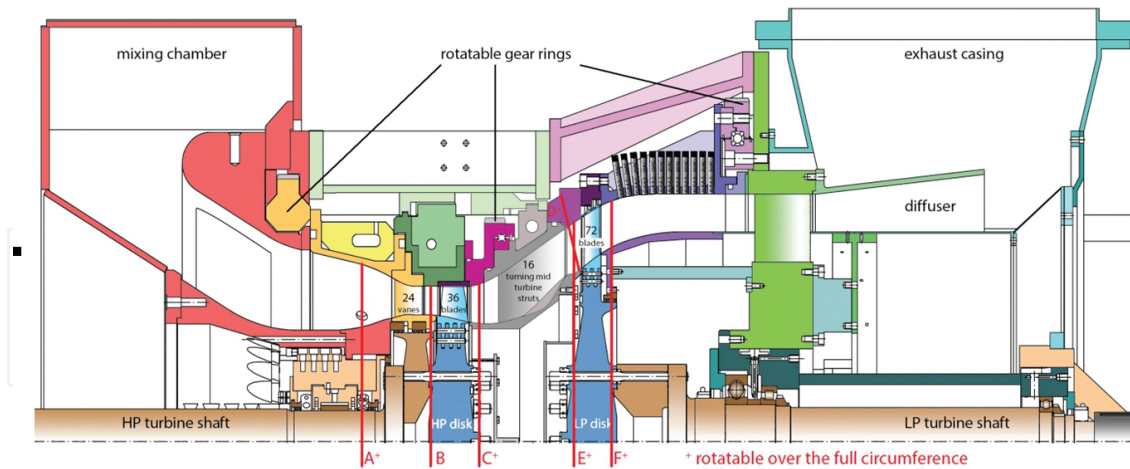


Figure 2. Meridional section of the TTTF.

Blading parameters					
	HP vane	HP blade	Strut C1/C2/C3	Splitter C3	LP blade
Vane/blade no.	24	36	16	32	72
$h / c_{ax}$	1.15	1.37	0.46/0.53	3.5	2.94
Tip gap	- Unshrouded -			-	Shrouded
Operating conditions ADP	C1	C2		C3	
$BPF_{HP}$ [kHz]	6.69	6.69		6.69	
$BPF_{LP}$ [kHz]	4.26	4.26		4.26	
Stage $p_t$ ratio HPT/ LPT	3/1.3	3/1.3		2.83/1.36	
Power [MW] HPT/ LPT	1.44/ 0.3	1.44/ 0.3		1.43/ 0.3	

Table 2. Blading parameters and operating conditions.

Configuration 1 (C1) consists of 16 turning struts. It has a non-dimensional length of about 3.5 ( $L_{ax}/h_{in}$ ) and an area ratio of 2. C1 was designed using a quite complex three-dimensional design of the strut and keeping rotationally symmetric endwall contours. The struts have a maximum thickness to chord ratio of 22% at about 25% of the axial chord length to provide enough space for service lines like oil pipes and for load carrying structures. Two major goals were set for the aero design of the second configuration (C2). Firstly, C2 has to be more aggressive than the first configuration and secondly, the LPT performance has to be unchanged, keeping the same pressure loss. For C2 also, 16 turning struts have been assembled. For all configurations the same high pressure stage and low pressure rotor have been used.

Therefore, the radial offset and the area ratio are the same for both setups but configuration C2 was designed to be 10% shorter than configuration C1. C2 has a non-dimensional length of 3.1. Close to the hub the axial gap between the strut trailing edge and the leading edge of the LPT is the same as for C1. However, that gap is 20% shorter at midspan and 50% at the casing, respectively. The vane is designed to produce minimum blockage and therefore, it should create minimum losses. Both struts give the possibility to lead through identical service lines. To avoid additional losses and provide same inflow conditions to the LP turbine as the configuration C1, non-axisymmetric endwall contouring was applied at the hub. The optimisation of endwall contour was performed using parameterization based on orthogonal basis perturbation functions. The third setup is based on the same geometry as C1, but 32 splitter vanes have been added for setup C3. Within each strut passage two non-lifting splitters are located. The splitter vanes have been numerically designed and represent a compromise between aerodynamic effectiveness and additional blockage, because it was required to use the same casing parts. Therefore, it was not possible to change the area to count for the additional blockage of the splitters.

### 2.3. Instrumentation

Five-hole probes with a probe head of 2.5 mm diameter have been applied. The probes were used in measurement plane C downstream of the rotor and in plane D downstream of the TEGV (see **Figure 1b**). The probes are calibrated in a Mach numbers range between 0.1 and 0.8 in 0.1 steps, yaw angles between  $-20^\circ$  and  $+20^\circ$  in steps of 4 deg, pitch angles between  $-16^\circ$  and  $+20^\circ$ , also in steps of  $4^\circ$ . Negative values of the yaw angle indicate a counter-rotating flow and negative values of the pitch angle indicate the flow direction towards the hub. A multi-parameter approximation correlates the calibration characteristics and the flow value to be measured.

The axial positions of measurement planes (marked with letters) can be seen in **Figure 1** for the STTF-AAAI and **Figure 2** for the TTTF. TEGV/Strut inlet plane is located downstream of the rotor trailing edge. TEGV exit plane can be found 55% of the axial chord length of the H-TEC TEGV downstream of its trailing edge and also 130% axial chord length of the reference TEC downstream. The measurement grid covers one TEGV or a strut pitch and about 95% passage height. The five-hole probe was traversed along radial lines. In each measurement point the probe has been aligned with the flow vector to reach the highest accuracy and further to ensure not to exceed the calibration range of the probe (with these probes, it would not have been necessary if one can ensure to be always within the calibration range).

In order to calculate the sound power (propagating downstream) from measured sound pressures, 12 flush mounted condenser microphones ( $1/4''$ ) at the hub and 12 at the casing have been applied. The microphones have been located in the rotatable acoustic measurement section that can be rotated  $360^\circ$  with arbitrary step size. In addition to these microphones one additional microphone was mounted at a stationary position downstream of the TEGV's as well as struts trailing edge and is used as a reference. The complete sound field was detected at the hub and the casing by traversing the section  $360^\circ$  in steps of  $2^\circ$ . Some more detailed

information about the acoustic measurement section is given in Moser et al. [6] and in Faustmann et al. [7].

### 2.3.1. Measurement uncertainty

The measurement system is made up by 11 multichannel pressure transducers PSI 9016 with a total amount of 176 channels and an accuracy of 0.05% full scale for pressure measurements. Four National Instruments Field Point FP-TC-120 eight-channel thermocouple input modules and one FP-RTD-122 resistance thermometer input module is used. **Table 3** shows the measurement uncertainties (within a 95% confidence interval) of the five-hole probe measurements. These values contain an error due to the multi-parameter approximation, random error and the systematic error of the pressure transducers. The difference between the positive and the negative direction is a result of the multi-parameter approximation. The measurement uncertainties of the static pressure and the total pressure at test rig inlet as well as at stage inlet are  $\pm 1$  mbar. Uncertainties for total pressure measurements up- and downstream of the TEGVs are also in the range of  $\pm 1$  mbar. The overall uncertainty of the total pressure loss coefficient  $\zeta$  is estimated to be about  $\pm 0.0014$ . The random fluctuation of rotational speed is below 0.2% of the current operating speed. Measurement uncertainty of the temperature measurement is about  $\pm 0.5$  K. The day-to-day variation of the operating parameters such as pressure ratio, corrected speed, rotational speed, total pressure and temperature at rig inlet has been below 0.5%.

Ma	+0.006	-0.003	[/]
$\alpha$	+0.5	-0.08	[°]
pt	+3.3	-3.0	[mbar]
p	+5.3	-5.2	[mbar]

**Table 3.** Measurement uncertainties of the five-hole probe.

## 3. Acoustic analysis theoretical background

The acoustic analysis consists of four constitutive parts:

- phase averaging and adaptive resampling;
- modal decomposition;
- azimuthal and radial mode analysis; and
- computation of sound power.

After performing a Fast Fourier Transformation the sound pressure can be described as sum of acoustical modes propagating along the duct at a specific frequency. These modes are able to propagate in circumferential as well as in radial direction depending on the cuton frequency.

### 3.1. Phase averaging and adaptive resampling

In order to determine the acoustic effects a phase locked averaging is done. For the two-spool rig the phase of one of the two rotors is chosen. A shaft encoder from the monitoring system generates a pulse per revolution signal indicating start and end of one revolution. Triggering the flow is performed according to the triple decomposition procedure, which characterize a single source of periodic unsteadiness [8].

$$p(t) = \bar{p} + \langle p \rangle + p'(t) \quad (1)$$

The time dependent pressure  $p(t)$  is composed as sum of the averaged pressure, the purely periodic component  $p$  associated with a coherent periodic structure and the random fluctuation  $p'(t)$  that is mainly associated with turbulence.

Each revolution is divided into a fixed number of samples in order to correct small rotational speed variations of the rotor shaft [9]. The average of the samples at the same phase gives the phase averaged values. That procedure is well established and allows the identification of structures correlated to the rotor rotational speed. For a two-spool rig all fluctuations of flow quantities induced by the other rotor are removed. Also, depending on which trigger signal is used for the analysis acoustic effects from the HP-rotor or the LP-rotor can be determined.

### 3.2. Modal decomposition

The acoustic field at any circumferential position can be written as superposition of several space and time dependent sound pressure waves (acoustic modes). The propagation of that pressure waves is described by the linearised wave equation  $\frac{1}{c^2} \frac{\partial^2 p}{\partial t^2} - \Delta p = 0$ . The solution of that equation is represented by the general expression (given in many publications, e.g. [10–14]):

$$p(x, r, \varphi, t) = \sum_{m=-\infty}^{\infty} \sum_{n=0}^{\infty} \left( A_{mn}^+ e^{ik_{mn}^+ x} + A_{mn}^- e^{ik_{mn}^- x} \right) f_{mn} \left( \sigma_{mn} \frac{r}{R} \right) e^{im\varphi} e^{i\omega t} \quad (2)$$

$A_{mn}^+$ ,  $A_{mn}^-$  are the complex modal amplitudes of order (m,n).  $k_{mn}^+$  and  $k_{mn}^-$  represent the axial wave numbers,  $\omega$  is the angular frequency. The modal shape factor  $f_{mn}$  depends on the eigenvalues of the Bessel function  $\sigma_{mn}$  and the geometry given by the hub-to-tip-radius ratio  $\frac{r}{R}$ .  $f_{mn}$  represents the solution of the Bessel differential equation, describing the radial acoustic field considering hard wall boundary conditions [15, 16] and is defined as:

$$f_{mn} \left( \sigma_{mn} \frac{r}{R} \right) = \frac{1}{\sqrt{F_{mn}}} \left( J_{mn} \left( \sigma_{mn} \frac{r}{R} \right) + Q_{mn} Y_{mn} \left( \sigma_{mn} \frac{r}{R} \right) \right) \quad (3)$$

$J_{mn}$  and  $Y_{mn}$  are the Bessel functions of  $m$ th order of first and second kind.  $Q_{mn}$  is also an eigenvalue and  $F_{mn}$  is a normalisation factor transforming the system from an orthogonal to an orthonormal eigensystem [15, 16].

The axial wave numbers depend on the local flow properties, such as axial Mach number  $Ma_{ax}$  and the swirl number  $\Omega$ . For the following investigations the swirl is approximated by a rigid body rotation of a steady flow, which leads to a modification of the wave number definition [17]:  $\tilde{k} = k - m \frac{\Omega}{c}$ . The axial wave numbers are then calculated as follows:

$$k_{mn}^{\pm} = \frac{\tilde{k}}{1 - Ma_{ax}^2} \left[ -Ma_{ax} \pm \sqrt{1 - (1 - Ma_{ax}^2) \frac{\sigma_{mn}^2}{\left( \tilde{k} R \right)^2}} \right] \quad (4)$$

Physical and geometrical conditions allow only the propagation of a certain number of specific mode combinations  $(m,n)$  along the duct. The axial wave number  $k_{mn}^{\pm}$  has to be real; otherwise the result of Eq. (2) will yield to an exponential sound pressure decay if  $k_{mn}^{\pm}$  is a complex number. The frequency at which a mode  $(m,n)$  is first able to propagate is defined by the cuton frequency:

$$(kR)_{mn} = \sqrt{1 - Ma_{ax}^2 \sigma_{mn}^2} + \frac{m\Omega R}{c} \quad (5)$$

The swirl factor  $\frac{m\Omega R}{c}$  shifts the cuton frequency to higher or lower values, depending on the sign of  $\Omega$ . Or in other words, for a specific frequency modes to be cut on are also shifted to higher or lower azimuthal mode orders  $m$ , hence the propagating mode distribution becomes asymmetric. The specific modes propagating through a duct downstream of a turbomachine stage result from the rotor-stator interaction and are specified by a simple mathematical relation proposed by Tyler and Sofrin [5]:

$$m = hB \pm kV; k = \dots, -2, -1, 0, +1, +2, \dots \quad (6)$$

$h$  represents the harmonic index (e.g. 1 for the first blade passing frequency, 2 for the second, etc.), and  $B$  and  $V$  are the number of rotor blades and the number of stator vanes, respectively. According to Eq. (1) it is possible to determine the interactions of the rotor with a complete

vane assembly by simply superimposing the effect of the single event. For a stator-rotor-stator assembly the modes can be predicted easily when extending Eq. (6).

$$m = hB \pm k_1 V_1 \pm k_2 V_2; k_{1,2} = \dots, -2, -1, 0, +1, +2, \dots \quad (7)$$

### 3.3. Azimuthal and radial mode analysis

The computation of the propagating sound field in a turbomachine is based on the determination of the amplitudes  $A_{mn}^\pm$  in Eq. (2). That means that the sound pressure at several axial and circumferential positions has to be measured first, e.g. by means of a microphone array. Then the radial mode analysis (RMA) described, e.g. in Holste and Neise [13], Tapken and Enghardt [15], and Enghardt et al. [12, 18] is applied. The RMA is a methodology used for the modal decomposition of an in-duct acoustic field. The data is used to reconstruct at specific times the instantaneous circumferential pressure distribution. The application of a spatial Fourier Transformation over this data set represents the first action and is called azimuthal mode analysis (AMA):

$$A_m(x, r) = \frac{1}{N_\varphi} \sum_{k=1}^{N_\varphi} p(x, r, \varphi_k) e^{-im\varphi_k} \quad (8)$$

In order to determine the complex amplitudes  $A_{mn}^\pm$  at a specific angular frequency  $\omega$  for each azimuthal mode  $m$  Eq. (2) can be written as [18, 19]:

$$A_m(x, r) = \sum_{n=0}^{\infty} \left( A_{mn}^+ e^{ik_{mn}^+ x} + A_{mn}^- e^{ik_{mn}^- x} \right) f_{mn} \left( \sigma_{mn} \frac{r}{R} \right) \quad (9)$$

For each azimuthal mode order  $m$  a linear equation system  $\mathbf{A}_m = \mathbf{W}_m \mathbf{A}_{mn}$  can be found. Since this equation system is (usually) highly overdetermined, a least-mean-square fit algorithm is used to solve that inverse problem.

### 3.4. Computation of sound power

Considering the energy carried by each individual mode in a hard walled duct, the effective sound power can be determined according to Morfey [17]:

$$A_m(x, r) = \sum_{n=0}^{\infty} \left( A_{mn}^+ e^{ik_{mn}^+ x} + A_{mn}^- e^{ik_{mn}^- x} \right) f_{mn} \left( \sigma_{mn} \frac{r}{R} \right) \quad (10)$$

The complex factor  $\alpha_{mn} = \sqrt{1 - (1 - \text{Ma}_{ax}^2) \frac{\sigma_{mn}^2}{(\bar{k}R)^2}}$  contains the definition of the cuton frequency.

## 4. Research on TECs

**Figures 3 and 4** show the sound power level (PWL) of different azimuthal mode orders  $m$  that are cuton. The PWL is evaluated for the first blade passing frequency (BPF) at the operating point approach. The black bars in both figures indicate the sound power level of sound waves propagating in flow direction  $PWL^+$  and the gray bars show the PWL of propagating waves against flow direction  $PWL^-$ . The dotted lines in the figures indicate the noise level of the measurements. The microphones are mounted on a vibrating machine which causes some systematic error.

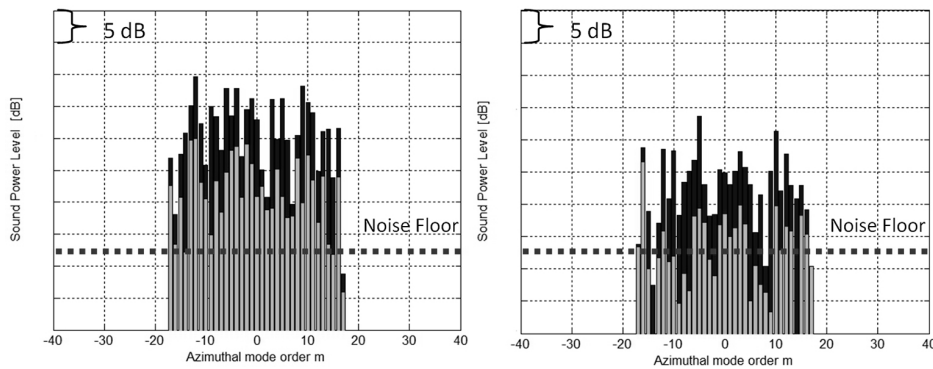


**Figure 3.** Sound power level of the reference TEC (left) and the leaned TEC (right).

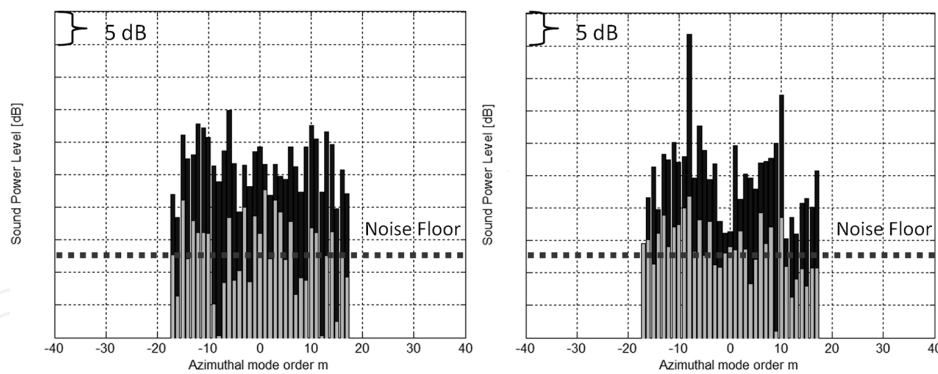


**Figure 4.** Sound power level of the inverse cutoff TEC (left) and the H-TEC (right).

Together with noise generated due to the evaluation technique and noise related to the measurement error the depicted level of overall noise floor can be assumed. **Figure 3** (left and right) shows the sound power level for the reference TEC and the leaned TEC, respectively. For the leaned TEC it can be seen that the overall PWL is about 8 dB lower than that of the reference TEC. Comparison of the inverse cutoff TEC (**Figure 4** (left)) with the reference TEC shows that  $PWL^\pm$  is about 5 dB lower for the inverse cutoff TEC. **Figure 3** (left) and **Figure 4** (right) show again the sound power level of different azimuthal mode order  $m$  that are cuton for the two TEC configurations (reference and H-TEC). Both are again evaluated for the first

BPF at operating point approach. The sound power level of the H-TEC configuration is about 1 dB lower than for the reference TEC. The noise reduction levels mentioned above also contain non-representative modes that belong to interaction modes with certain test rig components. These modes are created for example due to interaction of the sound field and the rear supporting struts at rig exit resulting in additional scattered modes. The difference in overall sound power level of the first BPF  $\Delta PWL = PWL - PWL_{ref}$  in and against flow direction as well as the sum of both is also given in **Table 4**.

Configuration	$\Delta PWL^+$	$\Delta PWL^-$	$\Delta PWL^\pm$
Reference TEC	0.0 [dB]	0.0 [dB]	0.0 [dB]
Leaned TEC	-8.1 [dB]	-7.8 [dB]	-8.1 [dB]
Inv. cutoff TEC	-5.2 [dB]	-8.2 [dB]	-5.4 [dB]
H-TEC	-0.6 [dB]	-8.6 [dB]	-1.0 [dB]

**Table 4.** Overall sound power level change for 1BPF.

Evaluating only engine relevant specific airfoil interactions shows a different trend than that depicted in **Table 4**. **Table 5** shows the azimuthal airfoil interaction mode orders (cuton modes) and also scattered modes calculated according to the equation of Tyler and Sofrin [5]. Mode orders higher than  $\pm 17$  are cut off. The main interaction mode of the rotor with the TEGV of the reference TEC, leaned TEC, and the H-TEC is cuton and clearly visible (see **Figures 3** and **4**).

Configuration	IGV-Rotor	Vane-Rotor	Rotor-TEC
Reference TEC	-4, +11	-6, +9	-12, +3
Leaned TEC	-4, +11	-6, +9	-12, +3
Inverse cutoff TEC	+11	Cutoff	Cutoff
H-TEC	+11	Cutoff	Cuton

**Table 5.** Airfoil interaction modes m.

**Table 6** shows how the sound power level changes (compared to the reference TEC) when considering only the main airfoil interaction modes given in **Table 5**. It can be seen that the inverse cutoff TEC achieves the highest reduction in sound power level (14 dB) of all investigated configurations. The leaned TEC reduces PWL by about 11 dB, but that means that it is still twice as “loud” as the inverse cutoff TEC. The aerodynamically optimized H-TEC even increases the sound power level by about 2 dB. At aero design point both TECs, the reference TEC and the leaned TEC have the same PWL. The aerodynamically optimized H-TEC

is about 1 dB louder than the reference TEC and the inverse cutoff TEC reduces PWL by about 3 dB which is half as loud as the reference TEC.

Configuration	$\Delta PWL^+$	$\Delta PWL^-$	$\Delta PWL^\pm$
Reference TEC	0.0 [dB]	0.0 [dB]	0.0 [dB]
Leaned TEC	-11.3 [dB]	-9.4 [dB]	-11.2 [dB]
Inverse cutoff TEC	-13.8 [dB]	-17.7 [dB]	-14.0 [dB]
H-TEC	+2.4 [dB]	-11.5 [dB]	+2.0 [dB]

**Table 6.** Sound power level change for 1BPF (airfoil interaction modes).

Considering only modes due to the TEC interaction and the scattering of modes at the TEC it can be seen that the inverse cutoff TEC even reduces PWL by 94 dB(!), because that mode is cut off. The leaned TEC has a reduced PWL of 11 dB and the H-TEC is again increasing the PWL by about 2 dB. In addition to the acoustic measurements five-hole probe measurements have been performed in order to compare the aerodynamics (loss estimation) of the three different TEC configurations with that of the state-of-the-art reference TEC.

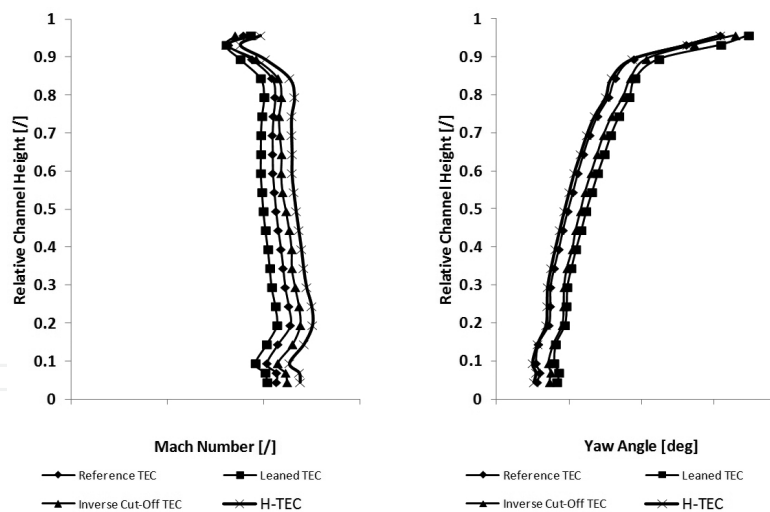


**Figure 5.** Mach number distribution (left) and yaw angle distribution (right) at TEC inlet.

#### 4.1. TEGV inlet flow: plane C

Comparing the TEGV inlet conditions of the different measurement campaigns for the different TEC configurations reveals only minor differences in flow quantities due to the upstream potential effect of the turbine exit guide vanes of TEC. The circumferentially mass averaged radial Mach number distribution show insignificant differences between the

configurations (**Figure 5** (left); 1 tick mark=0.1). Also the yaw angle is almost the same for all three configurations as can be seen in **Figure 5** (right) (1 tick mark=20°), the difference is also negligible. The largest difference between the TEC configurations can be seen at the tip above 90% channel height.

#### 4.2. TEGV outlet flow: plane D0, D

**Figure 6.** shows Mach number and yaw angle distribution downstream of the TEGVs. H-TEC and inverse cutoff TEC show a much more uniform distribution of the yaw angle at TEGV exit than the leaned and the reference TEC due to the higher vane count, thus, significantly improving the inflow conditions to a following component such as a mixer. Due to the fact that the inverse cutoff and the H-TEC does not consider additional blockage because of the higher TEGV count the Mach number in plane D could be possibly slightly higher than for the reference and the leaned TEC (same TEGV count).

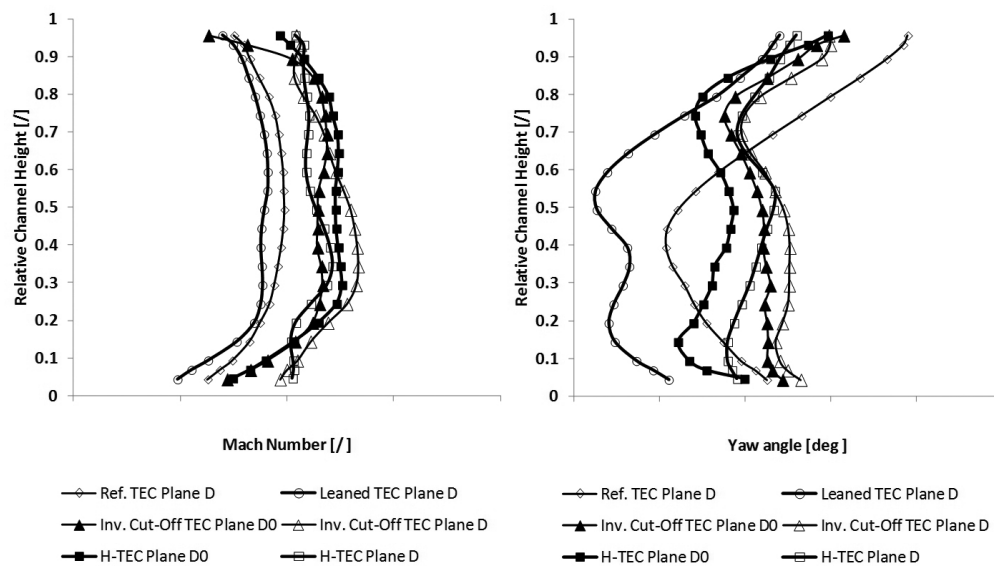


**Figure 6.** Mach number distribution (left) and yaw angle distribution (right) at TEC outlet.

#### 4.3. Loss estimation

A rough estimation of the total pressure loss coefficient  $\zeta = \frac{\bar{p}_{t,C} - \bar{p}_{t,D}}{\bar{p}_{t,C} - p_{ex}}$  from plane C upstream of the TEGVs to plane D downstream of the TEGVs is done. The total pressure has been mass averaged by means of the five-hole probe data. **Table 7** compares the change of total pressure loss of the three configurations. The loss coefficients have been normalised with the total pressure loss coefficient  $\zeta_{ref}$  of the reference configuration. Inverse cutoff, the leaned TEC as well as the H-TEC configuration show higher loss coefficients than the reference TEC. That means that all configurations produce higher losses for the acoustically important operating point approach and it seems that they are more sensitive at off design conditions. However,

the difference between the leaned and the inverse cutoff TECs is very small and within the measurement uncertainty.

Configuration	Total pressure loss $\frac{\zeta}{\zeta_{ref}}$	
	C-D	C-D0
Ref. TEC	1.0	-
Leaned TEC	~1.6	-
Inverse cutoff TEC	~1.6	~1.6
H-TEC	~1.3	~0.9

**Table 7.** Total pressure loss.

Further, it can be seen that the losses increase from plane D0 to D for the H-TEC. The losses are nearly constant for the inverse cutoff TEC from plane D0 to D. However, pressure loss measurements at aero design point showed a significant loss reduction from plane C to D for both, the aerodynamically optimised H-TEC and the inverse cutoff TEC when compared with the reference TEC  $\frac{\zeta}{\zeta_{ref}} = 0.9$ . A comparison between the leaned TEC and the reference TEC show similar losses so that  $\frac{\zeta}{\zeta_{ref}} \approx 1$ .

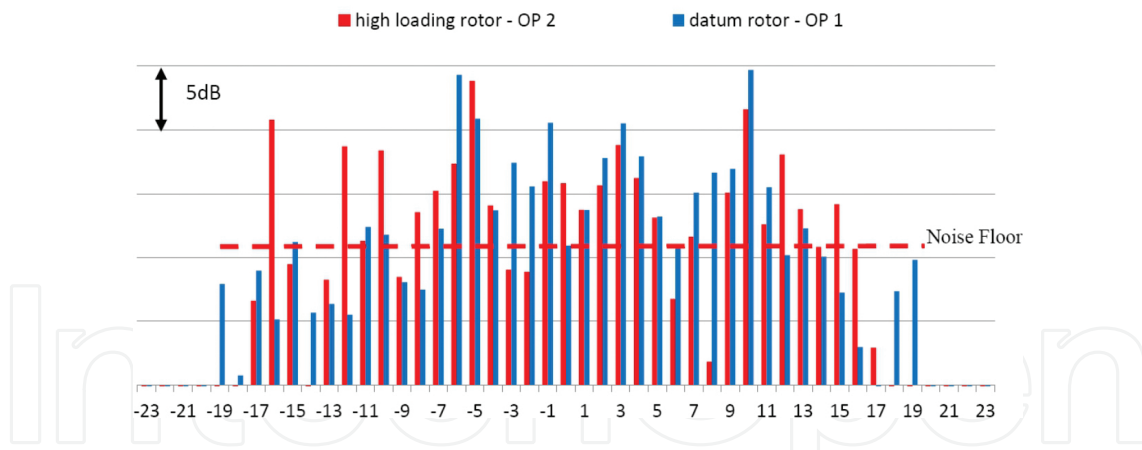


**Figure 7.** Comparison of modal PWL at LPT exit for two different stages; identical shaft power.

During the last decades a lot of institutions investigated the possibility to reduce engine weight by reducing the blade count of a low pressure rotor leading to highly loaded or even ultra-high-loaded turbine blades. Therefore, also the acoustical behaviour of such a rotor compared to a state-of-the-art design is investigated. At first, the results for the designated, acoustically relevant off-design point approach for the two rotors, called OP1 for the datum stage (higher rotational speed) and OP2 for the high loaded stage (lower rotational speed), are shown. Due to the change in loading of 20%, the resulting rotational speed for the two geometries differs by 10% (see **Table 1**). **Figure 7** shows a comparison of the sound power level of different

azimuthal mode orders evaluated for the first blade passing frequency (BPF) for the two different rotor setups. The cutoff criteria for the two operating points shows that for operating point 1 (OP1), the number of propagating modes is 39 ( $\pm 19$ ) whereas for operating point 2 (OP2), the number of propagating modes is only 35 ( $\pm 17$ ). Positive modes rotate against the rotational direction of the rotor and negative modes rotate in the same direction as the rotor. The figure also clearly shows that modes dominating the sound field are different for the two rotor configurations.

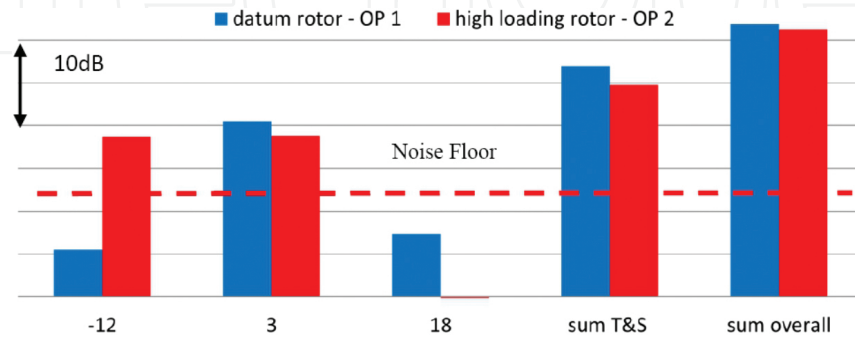


Figure 8. Comparison of modal PWL for propagating modes (rotor-TEGV-interaction).

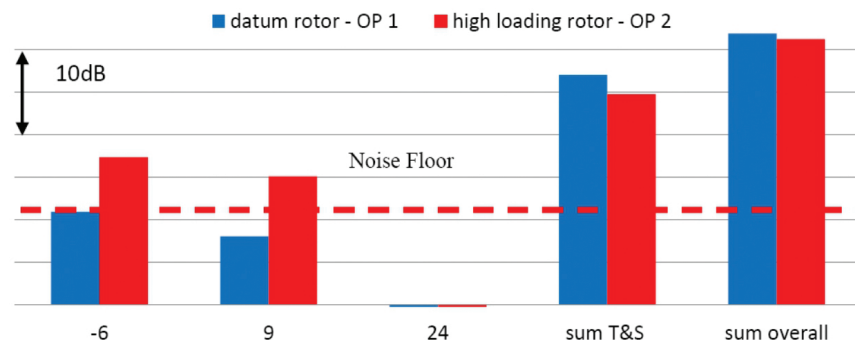


Figure 9. Comparison of modal PWL for propagating modes (rotor-stator-interaction).

The dominant modes for the OP1 with the datum rotor are the modes  $m=-6$  and  $+10$ , towering the next highest modes by approximately 4 dB. While the mode  $-6$  is predicted by Tyler and Sofrin, the mode  $m=+10$  could not be calculated. When, due to the higher loading of the second stage, the rotational speed is lowered, the modal distribution of the resulting flow field changes. The dominant mode for OP2 is the mode  $-5$ , that is, 2 dB higher than the second highest mode  $m=+10$ . The overall sound power level of the two configurations is shown in Figure 8. It can be seen that the PWL of the high loaded rotor with reduced rotational speed is reduced by 0.7 dB. Considering only the propagating modes predicted according to the theory of Tyler and Sofrin, the high loaded rotor shows a 2.5 dB lower PWL. The difference in power level between propagating modes according to Tyler and Sofrin and considering all modes found in the measurements is approximately 5 dB. The highest modes found in the analysis ( $m=+10$  for OP1 and  $m=-5$  for OP2) of the measurement data are not attributable to

Tyler and Sofrin. It is assumed that non-Tyler Sofrin modes are increased for the highly loaded stage. Also, the sound power due to airfoil lift is assumed to be higher for the high loaded rotor. In addition, **Figure 8** depicts the modal PWLs of the Tyler-Sofrin modes of the interaction between the rotor and the TEGVs.

The modes according to Tyler and Sofrin are  $m=-12$ ,  $m=+3$ , and  $m=+18$ . For the datum stage the highest amplitude for the rotor-TEGV interaction mode is for  $m=+3$ . For the high loaded stage both modes  $m=-12$  and  $m=+3$  show the same power level amplitude. Mode  $m=-18$  is cut off for the high load stage. Its contribution to the overall power level for the datum stage is negligible. **Figure 9** depicts the modal sound power levels of the stator-rotor interaction. The main interaction mode would be the mode  $m=+24$  that is cut off.

However, due to the small axial distance between stator and rotor the mode has not fully decayed and a scattering of that mode at the TEGVs is possible resulting in additional modes  $m=+9$  and  $m=-6$ . The remaining interactions between the rotor and the inlet guide vane of the testrig are depicted in **Figure 10**.

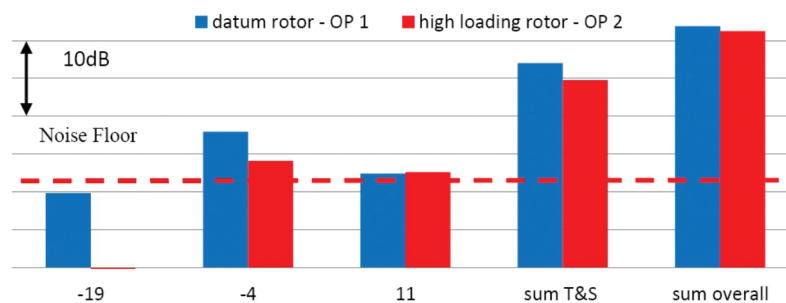


**Figure 10.** Comparison of modal PWL for propagating modes (rotor-IGV-interaction).

The mode  $m=-4$  has the highest PWL for both configurations, but is still approximately 7 dB lower than the sum of the Tyler and Sofrin modes. The mode  $m=11$  is significantly lower as well as the mode  $m=-19$ . This mode is only cut on and therefore able to propagate for the datum stage but is cut off and cannot propagate for the high loaded one. Comparing the different PWLs due to the interactions according to Taylor and Sofrin, the largest contributors to the overall PWL for the high loaded stage are interactions between the rotor and the TEGV as well as the mode  $m=-6$ , which is a rotor-stator interaction. For the datum stage the rotor-TEGV interaction ( $m=+3$ ) and the rotor-IGV interaction ( $m=-4$ ) are the main contributors to the overall sound power level.

#### 4.4. TEGV pressure loss estimation

Also for that investigation a rough estimation of the total pressure loss coefficient from plane C upstream to plane D downstream of the TEGVs is done by means of the five-hole probe data. **Table 8** shows the total pressure loss coefficients between both configurations. They have been normalised with the total pressure loss coefficient  $\zeta_{ref}$  of the reference configuration. The losses produced by the TEGV are slightly increased by about 16% for the high stage loading stage

upstream the TEGV than for the datum stage. It seems that flow structures from the rotor are mixed out in that TEC region and that the high loaded rotor produces flow structures resulting in higher mixing losses.

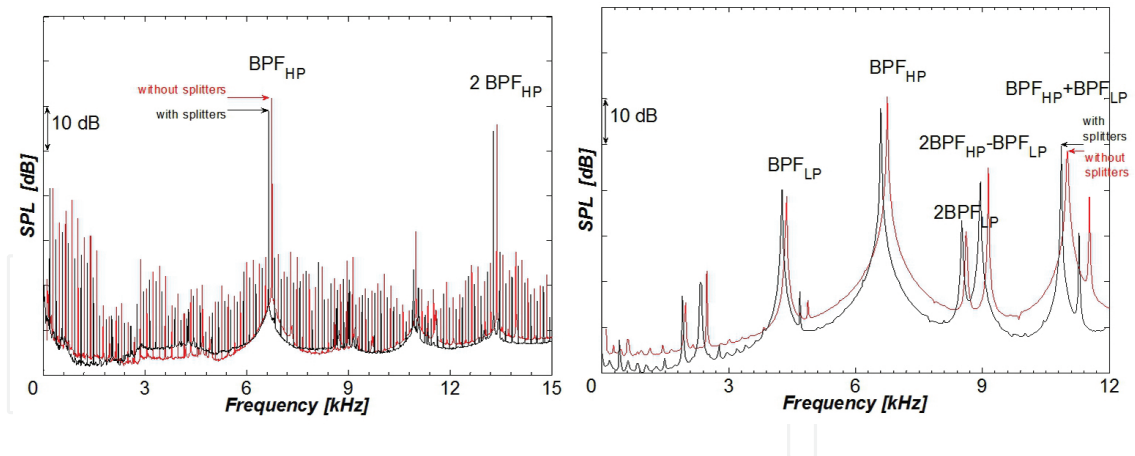
	Total pressure loss $\frac{\zeta}{\zeta_{ref}}$
Configuration	C-D
Datum stage	1.0
High loading stage	~1.16

Table 8. Total pressure loss.

## 5. Research on TCFs

### 5.1. Frequency spectra analysis

The frequency spectra in **Figure 11** (left and right) report the comparison between the two setups C1 (black) and C3 (red). **Figure 11** (left) shows that the highest amplitudes may be identified at the blade passing frequency of the HP rotor and its first harmonic. The red graph is shifted by 100 Hz for a better visibility.



**Figure 11.** Frequency spectra of the time-signal reconstructed by the HP trigger for the setup without splitters (red) and with splitters (black). Right: Frequency spectra of the microphone array for the sum of the BPF of the two rotors after rotor synchronic averaging; without splitters (red) and with splitters (black).

An opposite trend is observed at the  $BPF_{LP} + BPF_{HP}$ , where the amplitude is 10 dB lower than the one of the HP rotor alone. The amplitude at the frequency  $2BPF_{HP} - BPF_{LP}$  is almost the same as the logarithmic sum of the two rotors. Nearly 20 dB difference in the sound pressure level is observed between the amplitudes of the HP and the LP rotor. At  $BPF_{LP}$  the pattern of the peaks of the two different setups is like the one at  $BPF_{LP} + BPF_{HP}$ .

## 5.2. Azimuthal mode analysis BPF

An overview of the propagating modes is given in **Table 9** for the different blade passing frequencies. The modes are asymmetric, because the theoretical prediction taken into account for a swirl model [20].

Frequency	Range of the modes
$BPF_{HP}$	-44 : 8 : 36
$2BPF_{HP}$	-96 : 8 : 80
$BPF_{LP}$	-32 : 8 : 24
$2BPF_{LP}$	-64 : 8 : 48
$BPF_{LP} + BPF_{HP}$	-84 : 8 : 68

**Table 9.** Range for the propagating modes dependent on the BPF.

## 5.3. HP rotor noise

For explanation of the complex pattern of the sound field due to the vane/blade interactions, the modes predicted by Tyler and Sofrin at the  $BPF_{HP}$  are listed for the baseline setup (also given in Lengani et al. [21]): HP stator-HP rotor interaction creates modes  $m=36+k\Delta 24=..-36; -12; 12; 36$ . HP rotor-LP stator interaction results in modes  $m=36+k\Delta 16=..-28; -12; 4; 20; 36$ . The interaction of HP stator-HP rotor-LP stator creates modes  $m=36+k_1\Delta 24+k_2\Delta 16=..-44; -36; -28; -20; -12; -4; 4; 12; 20; 28$ . These modes may be identified in **Figure 12** on the left side for the baseline configuration C1. The picture shows the sound pressure level (SPL) for the  $BPF_{HP}$  in dB, for the different azimuthal mode orders  $m$ . In **Figure 12** propagating modes are marked with black bars. It is clear that the propagating mode ranges from mode -44 to +36. Mode orders  $m < -44$  and  $m > +36$  are cut off; however, a low amplitude is visible; hence they are not fully decayed within the duct. Furthermore, all modes with high amplitudes can be predicted according to Eq. (7) as linear combination of HP vane-HP blade-LP stator, and they are scattered by 8 (see also **Table 9**). Hence, noise emanated from the HP rotor has to be attributed to its interaction with the up-and downstream vanes. For the splitter setup the prediction of modes for the HP-rotor-LP stator interaction as well as for the HP stator-HP rotor-LP stator interaction can be done with different vane numbers. The LP vane count may be considered equal to 48 because of the 32 additional splitters. However the geometry of the splitters is not the same as the one of the struts and the splitter leading edge is far downstream in the strut passage, but for a first estimation it can be assumed that the interaction is similar. Therefore, the theory of Tyler and Sofrin is not fully satisfied but can be applied. For the interaction of HP stator-HP rotor-LP vanes the following modes may be predicted in the ideal case of assumed 48 identical LP vanes:  $m=36+k_1\Delta 24+k_2\Delta 48=..-36; -12; 12; 36$ ; Without this assumption and further considering that

LP vanes and splitters as separate vane rows (HP stator-HP rotor-LP vane-splitter interaction) the modes can again be obtained from this simple linear combination:

$$36 + k_1 \cdot 24 + k_2 \cdot 32 + k_3 \cdot 16 = \dots -44; -36; -28; -20; -12; -4; 4; 12; 20; 28; 36$$

The modes propagating in the case of the splitter setup are shown on the right side of **Figure 12**. The modes, which change significantly between the two setups, are labelled in the picture. Particularly, the power levels of modes  $m = -44$  and  $m = -28$  are significantly reduced by almost 20 dB for the configuration with splitters. Also the amplitude of mode  $m = +28$  is 10 dB lower. It should be noticed that these modes are not predicted assuming the ideal LP vane number of 48. It seems that the presence of splitter vanes changes the acoustic transmission of sound waves through the LP vanes for modes which are instead propagating for the baseline case. Further, modes from HP stator-HP rotor interaction are partially scattered at the leading edges of the 16 LP vanes and partially scattered further downstream in the LP vane passage at the 32 splitter leading edges. The modes mean value in the setup with the splitters is 5 dB lower than the one in the baseline setup.

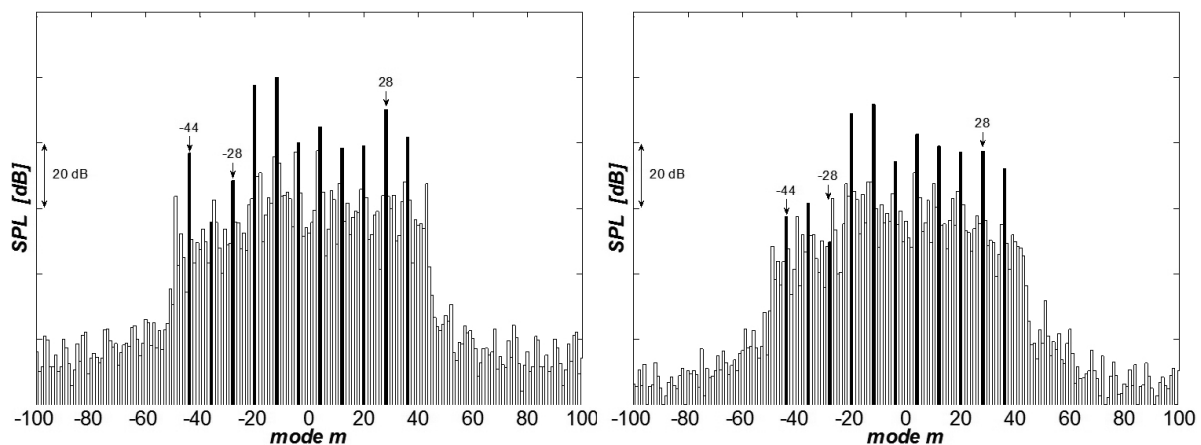


**Figure 12.** Azimuthal mode analysis of the flow with the HP trigger; without splitters (left) and with splitters (right).

#### 5.4. LP rotor noise

**Figure 13** depicts the sound power levels of the modal decomposition for the  $BPF_{LP}$ . This figure shows the baseline configuration on the left side and the splitter configuration on the right side. The interaction of the LP vane and the LP blade generates the following modes:  $m = -72 + k\Delta 16 = \dots -72; -56; -40; -24; -8; 8; 24$ . These modes can be clearly identified in the left side of **Figure 13**, and are additionally indicated in black. The highest sound pressure level is observed for mode  $m = -24$ . In-between  $-24 < m < 24$  other modes are blackened (e.g.  $m = -16, 0, +16$ ) that can be predicted when the linear combination of LP vane and blade additionally considers the interaction with the HP vane ( $-72 + k_1\Delta 16 + k_2\Delta 24$ ). However, the interaction between the HP vane and LP blade is weak (e.g. there is a difference of more than

20 dB between mode  $m = -24$  and  $m = -16$ ). Modes -72, -56, and -40 are still visible in the figure. These modes are generated by the LP rotor itself and by the LP stator-LP rotor interaction. However, those modes are cut off and therefore have a lower amplitude than the cuton modes. The cutoff modes will decay further downstream of the duct. In the case of the splitter setup (right side of **Figure 13**), again a different LP vane count may be considered. Ideally, the LP vane-LP rotor interaction would consist of the modes:  $m = -72 + k\Delta 48 = \dots -72; -24; 24$ . Mode  $m = -24$  has still the highest amplitude; however it is now in the same order of magnitude of the amplitude of mode  $m = -8$ . In the assumed ideal case of the splitter setup, mode  $m = -8$  should not be there. However, as observed by Spataro et al. [22, 23] the unsteady effects induced by strut and splitter vane wakes differ considerably downstream of the LP rotor. The modes generated due to the interaction of the 48 LP vanes with the LP blades may be predicted when the modes are scattered at the 16 struts (e.g. mode  $m = -8$  is obtained adding the 16 vanes to mode -24). In the case of the splitter setup, the mode  $m = -8$  is more than 20 dB higher than in the baseline case. Also the sound pressure level of the modes generated due to the interaction HP vanes-LP vanes-LP-rotor is altered. It seems that the splitter design shifts the important modes to lower orders (e.g. mode -8 which was hardly identifiable for the baseline setup). As can be seen in the mean spectrum (**Figure 11** (right)), the modes mean value is almost 3 dB lower for the baseline configuration.

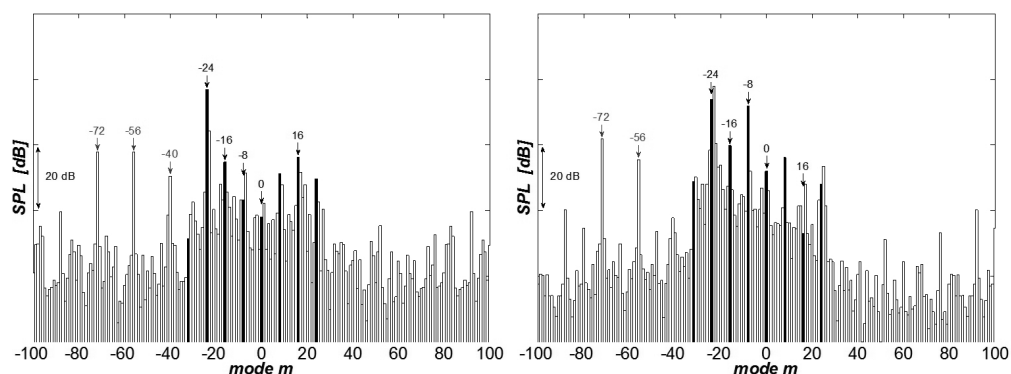


**Figure 13.** Azimuthal mode analysis of the flow with the LP trigger; without splitters (left) and with splitters (right).

Also for the splitter setup the modes  $m = -72$ ,  $-56$  are cut off as previously discussed for the baseline design. Mode  $m = -40$  is significantly reduced by more than 20 dB in the splitter configuration. The high sound pressure level at the  $BPF_{LP}$  may be due to the effect of “shifting” modes towards lower orders and not necessarily to an enhanced unsteady interaction. Unsteady measurements by means of a fast response aerodynamic pressure probe downstream of the LP rotor reported in Spataro et al. [23] revealed that the unsteady pressure fluctuations, evaluated for the LP rotor phase, are of comparable order of magnitude for both setups.

In **Figure 14** the sound power levels of the modal decomposition is shown for the sum of the blade passing frequencies of the two rotors ( $BPF_{LP} + BPF_{HP}$ ) for the baseline setup (left) and the setup with splitters (right). The modes mean value is almost the same for both setups.

However, there are some predominant modes clearly visible. Its amplitudes changing up to 23 dB and results from stator/rotor/stator/rotor interaction. Although mode  $m = -28$  has one of the highest sound power levels for the baseline setup, its amplitude is significantly reduced for the splitter design. But in the case of the splitters, other modes like  $m = -20$  and  $m = -4$  appear, with amplitudes that are 20 dB and 14 dB, respectively, higher than in the baseline setup. Therefore the sound pressure level of both setups is almost the same for that specific frequency (sum of the blade passing frequencies of the two rotors). The largest reduction of the modes mean amplitude for the splitter setup is associated to the HP rotor. There is a 5 dB lower amplitude at the  $BPF_{HP}$  compared to the baseline design. At  $2BPF_{HP}$  the results and trends of the azimuthal mode analysis are similar. A sound pressure level reduction of 4 dB was achieved with the splitter design. In contrast, the sound pressure level at  $BPF_{LP}$  and  $2BPF_{LP}$  is 3 dB lower for the setup without splitters, and at the  $BPF_{LP} + BPF_{HP}$  it is nearly the same in both cases.

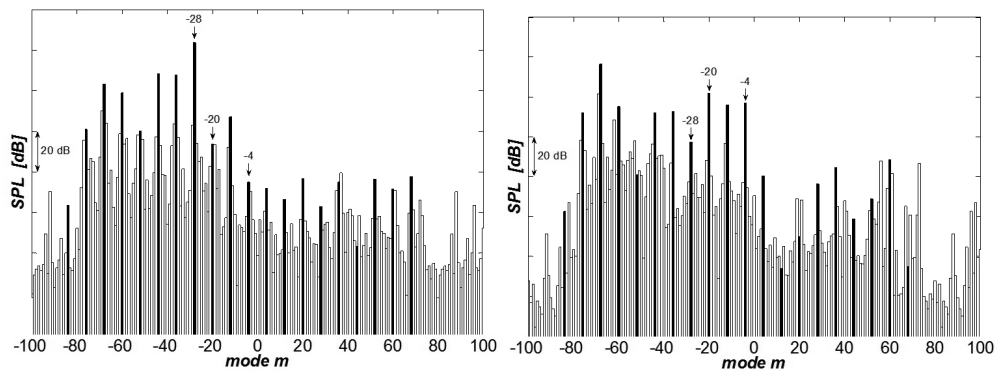


Figure 14. Azimuthal mode analysis of the flow with the two triggers; without splitters (left) and with splitters (right).

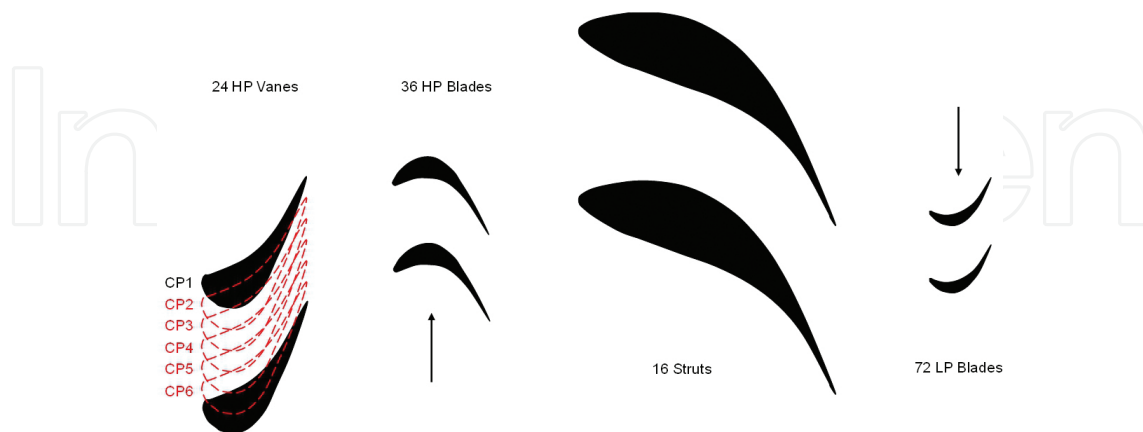
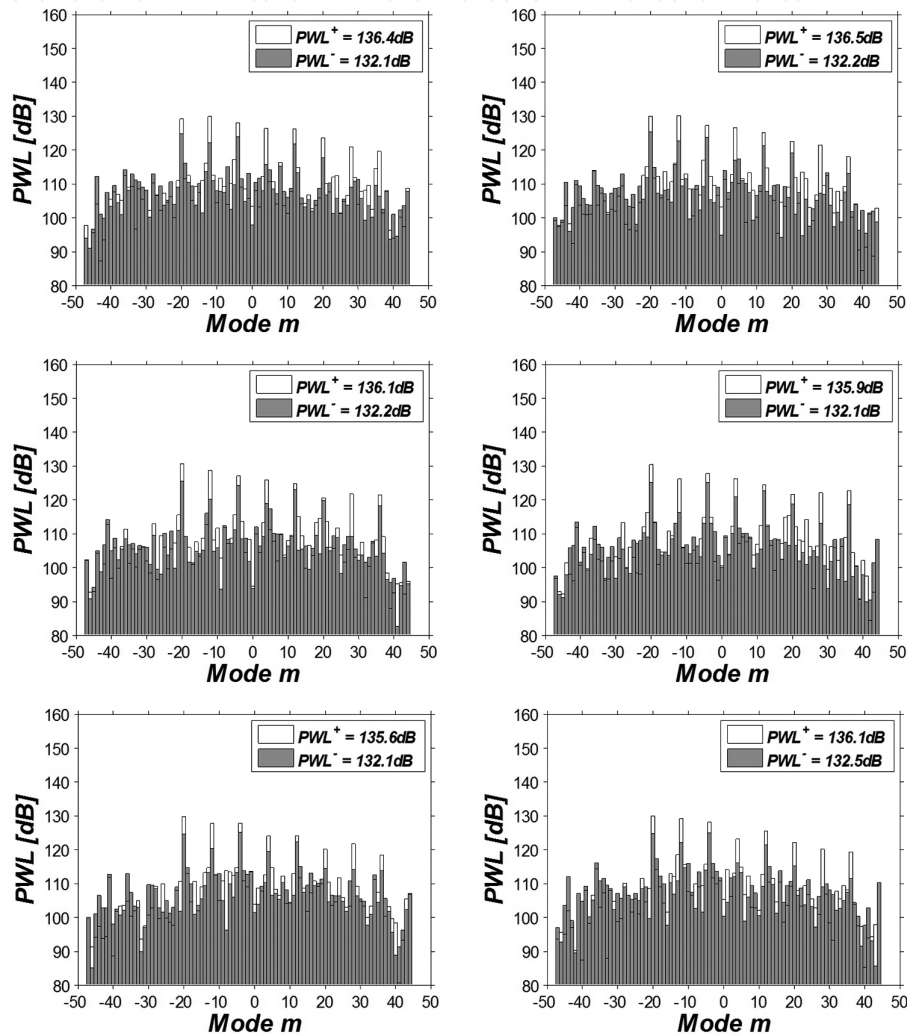


Figure 15. Section of the HP and LP stage showing the different clocking positions.

The comparison of the baseline setup C1 and the shortened setup C2 showed an increase of the sound pressure level between 5 and 9 dB dependent on the operating point. Especially the

interaction modes between the struts and the LP rotor increase due to the 10% shortening of the duct length.

As a next step the influence of airfoil clocking on the acoustics was investigated. The results of this investigation of noise generation and propagation for different clocking positions (CP) of the HP vanes and the struts are presented. A meridional section presenting the six vane-vane positions can be found in **Figure 15**.



**Figure 16.** Radial mode analysis with reference to the HP trigger.

The sound power levels for  $BPF_{HP}$  both in positive (gray bars in **Figure 16**) and in negative (white bars in **Figure 16**) flow direction were calculated and plotted for all the radial modes over the azimuthal modes at the abscissa. Furthermore an overall sound power level was determined by logarithmic addition for both directions of propagation. Further, **Figure 16** shows the sound power level in decibel (dB) over the propagatable azimuthal modes  $m$  summed over the radial mode order  $n$  in the up- and downstream direction for all clocking positions (CP1–CP6).

Several interaction modes are clearly visible in the figures. The amplitudes of these significant modes are 20 dB larger than those of the non-interaction modes. In particular, the modes  $m = -20$  and  $m = -12$  are dominant for all clocking positions except CP4 here the mode  $m = -4$  is higher than  $m = -12$ . Clocking position CP4 is that relative stator-stator position, where the sum of the most significant modes has its minimum. For the following discussion only the six dominating modes with the highest sound power levels are considered. With this analysis of certain modes the origin of a higher or a lower overall sound power level dependent on the clocking position can be determined. The most significant modes, which can be derived from different stator/rotor/stator interactions that can be predicted with Eq. (6) or Eq. (7), are selected and compared for all the different clocking positions. These interaction modes have the most influence on the overall sound power level, because if the difference between two incoherent sound signals is larger than 10 dB, the acoustic source with the smaller level has no noticeable influence on the sum of the power levels. The following significant azimuthal interaction modes (HP stator, HP rotor, and TMTF) were predicted:  $m = 36 + k_1 \Delta 24 + k_2 \Delta 16 = \dots -20; -12; -4; 4; 12; 20; \dots$ . Mode  $m = -20$  has the highest amplitude. This mode rises over the first three clocking positions (see **Figure 17**) reaching its maximum at clocking position 3, which is close to the optimum aerodynamic clocking position.

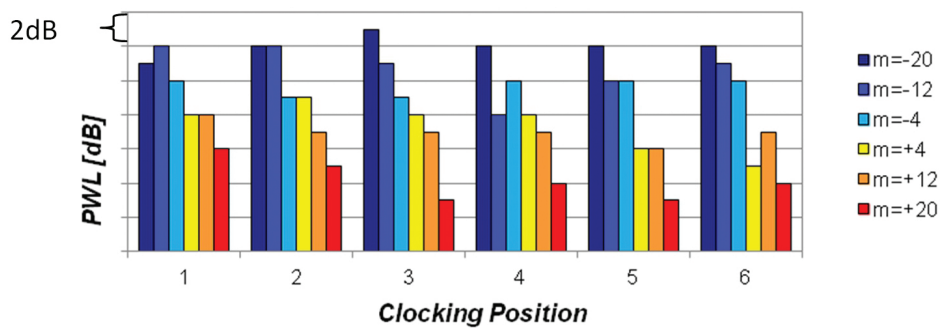


**Figure 17.** Six most dominant modes at seven different clocking positions.

Defining the optimum aerodynamic clocking position was performed by means of pre-test CFD calculations. In that way, most of the wakes of the HP stator impinge on the leading edges of the TMTF struts [24]. It is important that mode  $m = -20$  can only be predicted by the interactions of HP stator, HP rotor and the TMTF. It is assumed that this particular mode originates from an effect where the TMTF plays a significant role. That means that the wakes of the HP stator impinge on the leading edges of the struts and the flow through the strut passage remains more or less undisturbed. However, the flow downstream the turning mid turbine frame shows larger differences of flow quantities between the wake and the main passage flow. By changing the relative vane-vane position (=clocking also known as stator indexing) to the fourth clocking position the amplitude of  $m = -20$  is reduced. For the next two clocking positions 5 and 6 the sound power level remains almost the same. The high sound power level of mode  $m = -20$  is due to the vane/rotor/strut interaction. However, this mode is neither predicted by the HP stator-HP rotor interaction nor by the HP rotor/TMTF interaction. The unsteady interaction of the HP-stage is scattered by the downstream turning struts in the

flow path. Mode  $m = -20$  is generated by the scattering of the HP-stage interaction at the TMTF. **Figure 17** shows that the sound power levels of mode  $m = -12$  decrease from clocking position 1 to 4 and increase again from clocking position 4 to 6. The minimum sound power level can be seen at clocking position 4. The mode  $m = -12$  is either generated by the HP stator-HP rotor interaction or by the HP rotor-TMTF interaction. In case of mode  $m = -12$  the strongest influence of the different clocking positions can be determined. This particular mode is reduced by 4 dB when changing the relative vane-vane position from CP1 to CP4. For the modes  $m = +12$  and  $m = +20$  a similar trend to mode  $m = -12$  can be observed. These modes also show significant changes of the sound power levels of up to 3 dB due to different relative positions of the HP vanes and the TMTF struts. Both modes reach their minimum sound power level at clocking position 5, whereas the level of the amplitudes is decreasing from 1 to 4. The mode  $m = +12$  is generated by the interaction of the HP vanes and the HP blades but also by scattering of the HP stage interaction modes at the TMTF. The mode  $m = +20$  is always generated in conjunction with the TMTF-vanes, either with the HP rotor or with the HP stage. While the amplitude of mode  $m = -4$  seems to be almost constant for all clocking positions, mode  $m = +4$  changes from CP2 to CP6 by 4 dB, whereas at the last clocking position the amplitude of  $m = +4$  has its lowest value. Both modes are the result of the interaction of the HP-stage and the TMTF. Summing up the sound power levels (depicted in **Figure 17**) reveals that there is a minimum sound power at clocking position CP4. A difference in sound power level of app. 2 dB between the acoustically best (CP4) and worst (CP2) clocking position is observed.

## 6. Conclusions

Three different turbine exit casings with different turbine exit guide vane (TEGV) designs have been compared to a state-of-the-art (reference) TEGV design. The possible reduction of sound power levels when applying the different designs and a rough estimation of the aerodynamic losses have been presented. When comparing the overall reduction of PWL (only considering the main airfoil interaction modes) it was revealed that the acoustically optimised inverse cutoff TEC has the largest reduction of sound power level of 14 dB. The aerodynamically optimised H-TEC even increases the overall sound power level by about 2 dB. The leaned TEC also decreases the PWL by about 11 dB, but is still as twice as loud as the inverse cutoff TEC. However, for the operating point approach the aerodynamic losses are increased for all TEC designs. The losses measured at the aero design point are lower for the aerodynamically optimised H-TEC and the inverse cutoff TEC than for the reference TEC. Both, the H-TEC and the inverse cutoff TEC provide a much more uniform yaw angle distribution downstream of the trailing edge. These results give confidence that it is possible to design an aerodynamically and acoustically optimised TEC. Further, the effect of a change in stage design onto a TEGV with a compound lean was investigated and presented in this chapter. It was shown that while keeping the shaft power constant, the noise emissions downstream of the TEGV can be reduced by 0.7 dB for the given geometry and operating point. This decrease in sound power level is not caused by a decrease in interactions, but rather by acoustic modes not attributable to these interactions. The overall sound power level of the modes is increased by 0.3 dB. When having

the same rotational speed for the high loaded stage and the datum stage, the main interaction modes are identical. In addition to that main modes, several additional modes are found, that have been leading to an overall increase in sound power level. The TEGV inlet flow show only minor differences between the two stage designs. The main change occurs in the tip region. The main flow features of the TEGV exit flow remain identical. But it was observed that the shape of the wake changes due to the changes in the rotor tip leakage flow upstream of the TEGV. This increases the total pressure loss of the TEGV by approximately 16%.

Because of the possible significant reduction of the generated noise at the turbine exit casing noise from more upstream engine components such as the turbine centre frame can become a problem. Therefore, the noise generation between high pressure turbine, turbine centre frame, and low pressure turbine was investigated. Three different setups have been compared to each other. A baseline case C1 is designed with turning struts. A second design C2 reduces the axial length of the turbine centre frame. The third design C3 is characterized by the presence of two non-lifting splitters embedded into the strut passage. In the frequency spectra, the peak at the  $BPF_{HP}$  is 3 dB lower for the splitter setup. In the azimuthal mode analysis the difference is even higher. The sound power level decreased 5 dB at the  $BPF_{HP}$  for the setup with the splitters. Additionally, both the frequency spectra and the azimuthal mode analysis have shown that the noise generated by the LP rotor is slightly higher for the setup with the splitters. The splitter design is suppressing some modes, while others are scattered or are even more pronounced than in the baseline configuration. The splitters reduce the overall noise propagation by 5 dB acting as a cutoff filter for the HP stage rotor. The comparison of the baseline setup C1 and the shortened setup C2 showed an increase of the sound pressure level between 5 and 9 dB dependent on the operating point. Additionally, an experimental investigation in order to explore the potential of different vane-vane clocking positions on the noise generation and propagation was conducted. The six most significant modes have been analyzed regarding their sound power levels for the six clocking positions. The modes varied in their absolute values for the sound power and also their trend over the clocking positions changed. An optimum clocking position for acoustics was found, but it does not to coincide with the optimum aerodynamic clocking position. The difference of the overall sound power level for the six most relevant modes between the optimum acoustic clocking position (CP4) and the aerodynamic one (CP3) is about 2 dB.

## 7. Nomenclature

### Abbreviations

ACARE	Advisory Council for Aeronautics Research in Europe
AMA	Azimuthal mode analysis
BPF	Blade passing frequency

C1, C2, C3	Configuration 1, 2, 3
CP1,...,CP6	Clocking position 1 to 6
EGV	Exit guide vanes
HP	High pressure
HPT	High pressure turbine
IGV	Inlet guide vanes
LP	Low pressure
LPT	Low pressure turbine
OP1, OP2	Operating point 1, 2
PWL	Sound power level
RMA	Radial mode analysis
SPL	Sound pressure level
STTF-AAAI	Subsonic test turbine facility for aerodynamic, acoustic, and aeroelastic investigations
TCF	Turbine centre frame
TEC	Turbine exit casing
TEGV	Turbine exit guide vanes
TMTF	Turning mid turbine frame
TTTF	Transonic test turbine facility
T&S	Tyler and Sofrin modes

**Symbols**

A	Complex amplitude
B	Number of blades
c	Velocity, speed of sound
F	Normalisation factor
f	Modal shape factor
h	Channel height
h	Harmonic index, integer number
i	Imaginary unit
J	Bessel function of first kind
k	Wave number
k	Integer number
Ma	Mach number
m	Azimuthal mode order
P	Sound power

p	Pressure
Q	Eigenvalue of the Bessel function
Re	Reynolds number
r	Radius
R	Outer radius
t	Time
V	Number of vanes
Y	Bessel function of second kind
$\alpha$	Yaw angle
$\alpha$	Axial wave number considering cuton frequency
$\alpha$	Circumferential position
$\omega$	Angular frequency
$\Omega$	Angular frequency of swirl
$\sigma$	Eigenvalues of the Bessel function
$\rho$	Density (air)
$\zeta$	Pressure loss coefficient
$\Delta$	Laplace operator, delta
$\diamond$	Deterministic periodic component

#### Index

1,2,3,..	Stage count
ax	axial
C, D	Measurement planes
ex	Exhaust casing
H-TEC	High lift design TEC
inv.	Inverse cut-off TEC
leaned	Leaned TEC
m	Azimuthal mode order
n	Radial mode order
ref	Reference
t	Total

#### Superscripts

$\ominus^-$	Time averaged properties
$\ominus^{\sim}$	Ensemble averaged properties, modified wave number
$\ominus'$	Stochastic fluctuations

- ⊖ Mass averaged
- + Propagation in flow direction
- Propagation against flow direction

## Author details

Andreas Marn<sup>1\*</sup>, Christian Faustmann<sup>2</sup> and Thorsten Selic<sup>3</sup>

\*Address all correspondence to: andreas.marn@tugraz.at

1 Institute for Thermal Turbomachinery and Machine Dynamics, Graz University of Technology, Graz, Austria

2 Audi AG, Ingolstadt, Germany

3 Elin Motoren GmbH, Preding/Weiz, Austria

## References

- [1] D. Sutliff, Rotating Turbofan Duct Mode Measurement System, "Proceedings of 9th National Conference on Noise Control Engineering", October 2005.
- [2] Broszat D, Kennepohl F, Tapken U, Moser M, Heitmeir F. Validation of an Acoustically 3D-Designed Turbine Exit Guide Vane. In: Proceedings of the 16th AIAA/CEAS Aeroacoustics Conference, Stockholm, Sweden; June 8-9; 2010. DOI: 10.2514/MAERO10
- [3] Broszat D, Selic T, Marn A. Verification of the Inverse Cut-Off Effect in a Turbomachinery Stage. Part 1 – Numerical Results. In: Proceedings of the 18th AIAA/CEAS Aeroacoustic Conference, Colorado Springs, Colorado, USA; June 4-6; 2012. DOI: 10.2514/MAERO12
- [4] Broszat D, Selic T, Marn A. Verification of the Inverse Cut-Off Effect in a Turbomachinery Stage. Part 2 – Comparison to Experimental Results. In: Proceedings of the 19th AIAA/CEAS Aeroacoustic Conference, Berlin, Germany; May 27–29; 2013. DOI: 10.2514/MAERO13
- [5] Tyler J M, Sofrin T G. Axial Flow Compressor Noise Studies. SAE Transactions. 1962;70:309-332.
- [6] Moser M, Tapken U, Enghardt L, Neuhaus L. An Investigation of Low Pressure Turbine Blade-Vane Interaction Noise: Measurements in a 1.5-Stage Rig. Proceedings of the

Institution of Mechanical Engineers, Part A: Journal of Power and Energy. 2009;223(6): 687-695. DOI: 10.1243/09576509JPE823

- [7] Faustmann C, Lengani D, Spataro R, Marn A, Göttlich E, Heitmeir F. Experimental Investigation of the Noise Generation and Propagation for Different Turning Mid Turbine Frame Setups in a Two-Stage Two-Spool Test Turbine. In: Proceedings of the ASME Turbo Expo, San Antonio, Texas, United States of America; June 3–7; 2013. DOI: 10.1115/GT2013-95698
- [8] Hussain W, Reynolds A. The Mechanics of an Organized Wave in Turbulent Shear Flow. *Journal of Fluid Mechanics*. 1970;41:241-258. DOI: 10.1017/S0022112070000605
- [9] Lengani D, Santner C, Spataro R, Göttlich E. Analysis Tools for the Unsteady Interactions on a Counter-Rotating Two-Spool Turbine Rig. *Experimental Thermal Fluid Science*. 2012;42:248-257. DOI: 10.1016/j.expthermflusci.2012.05.010
- [10] Enghardt L, Neuhaus L, Lewis C. Broadband Sound Power Determination in Flow Ducts. In: Proceedings of the 10th AIAA/CEAS Aeroacoustic Conference, Manchester, United Kingdom; May 10–12; 2004. DOI: 10.2514/MAERO04
- [11] Enghardt L, Tapken U, Kornow O, Kennepohl F. Acoustic Mode Decomposition of Compressor Noise Under Consideration of Radial Flow Profiles. In: Proceedings of the 11th AIAA/CEAS Aeroacoustic Conference, Monterey, California, United States of America; May 23-25; 2005. DOI: 10.2514/MAERO05
- [12] Enghardt L, Tapken U, Neise W, Kennepohl F, Heinig K. Turbine Blade/Vane Interaction Noise: Acoustic Mode Analysis Using In-Duct Sensor Arrays. In: Proceedings of the 7th AIAA/CEAS Aeroacoustic Conference, Maastricht, Netherlands; May 28–30; 2001. DOI: 10.2514/MAERO01
- [13] Holste F, Neise W. Noise Source Identification in a Propfan Model by Means of Acoustical Near Field Measurements. *Journal of Sound and Vibration*. 1997;203(4):641-665. DOI: 10.1006/jsvi.1996.0890
- [14] Laguna J D, Barteld M, Seume J. Impact of Swirl on the Sensitivity of the Radial Mode Analysis in Turbomachines. In: Proceedings of the ASME Turbo Expo, San Antonio, Texas, United States of America; June 3–7; 2013. DOI: 10.1115/GT2013-95460
- [15] Tapken U, Enghardt L. Optimization of Sensor Arrays for Radial Mode Analysis in Flow Ducts. In: Proceedings of the 12th AIAA/CEAS Aeroacoustic Conference, Cambridge, Massachusetts, United States of America; May 8–10; 2006. DOI: 10.2514/MAERO06
- [16] D. Sutliff, „Rotating Turbofan Duct Mode Measurement System,“ *Proceedings of 9th National Conference on Noise Control Engineering*, Minneapolis, Minnesota, United States of America; October 2005.
- [17] Morfey C. Sound Transmission and Generation in Ducts with Flow. *Journal of Sound and Vibration*. 1971;14(1):37-55. DOI: 10.1016/0022-460X(71)90506-2

- [18] Enghardt L, Zhang Y, Neise W. Experimental Verification of a Radial Mode Analysis Technique Using Wall-Flush Mounted Sensors. *Journal of The Acoustical Society of America*. 1999;105(2):1186–1187. DOI: 10.1121/1.425598
- [19] Sijtsma P, Zillmann J. In-Duct and Far-Field Mode Detection Techniques. In: *Proceedings of the 13th AIAA/CEAS Aeroacoustic Conference, Rome, Italy; May 21-23; 2007*. DOI: 10.2514/MAERO07
- [20] Taddei F, De Lucia M, Cinelli C, Schipani C. Experimental Investigation of Low Pressure Turbine Noise: Radial Mode Analysis for Swirling Flows. In: *Proceedings of 12th International Symposium on Unsteady Aerodynamics, Aeroacoustics & Aeroelasticity of Turbomachines, London, United Kingdom; 2009*.
- [21] Lengani D, Santner C, Spataro R, Paradiso B, Göttlich E. Experimental Investigation of the Unsteady Flow Field Downstream of a Counter-Rotating Two-Spool Turbine Rig. In: *Proceedings of the ASME Turbo Expo, Copenhagen, Denmark; June 11-15; 2012*. DOI: 10.1115/GT2012-68583
- [22] Spataro R, Göttlich E, Lengani D, Faustmann C, Heitmeir F. Development of a Turning Mid Turbine Frame with Embedded Design-Part I: Design and Steady Measurements. In: *Proceedings of the ASME Turbo Expo, San Antonio, Texas, United States of America; June 3-7; 2013*. DOI: 10.1115/GT2013-95279
- [23] Spataro R, Göttlich E, Lengani D, Faustmann C, Heitmeir F. Development of a Turning Mid Turbine Frame with Embedded Design-Part II: Unsteady Measurements. In: *Proceedings of the ASME Turbo Expo, San Antonio, Texas, United States of America; June 3-7; 2013*. DOI: 10.1115/GT2013-95280
- [24] Schennach O, Pecnik R, Paradiso B, Göttlich E, Marn A, Woisetschläger J. The Effect of Vane Clocking on the Unsteady Flow Field in a One-and-a-Half Stage Transonic Turbine. *Journal of Turbomachinery*. 2008;130:031022-1 – 031022-8. DOI: 10.1115/1.2777199

IntechOpen